Article | Received 15 September 2026; Revised 29 October 2026; Accepted 4 November 2026; Published 18 November 2026
https://doi.org/10.55092/aimat20260015

Unraveling intermediate–active site interaction mechanisms for tuning CO_2 reduction selectivity via ML-DFT

Tianxiang Li[1], Yikai Yu[1], Hao Ren[1], Houyu Zhu[1], Wen Zhao[1], Yuhua Chi[1,*], Yong Liu[2] and Wenyue Guo[1]

[1] School of Materials Science and Engineering, Shandong Key Laboratory of Intelligent Energy Materials, China University of Petroleum (East China), Qingdao, China
[2] Department of Chemistry, University of Colorado Denver, Denver, USA

* Correspondence author; E-mail: chiyuhua@upc.edu.cn.

Highlights:

- DFT and ML reveal metal-dependent CO_2RR selectivity on M@N-WS_2 catalysts.
- ICOHP links carbon–metal bond strength to product selectivity.
- SISSO establishes an interpretable rule for rapid selectivity prediction.

Abstract: Selective photocatalytic CO_2 reduction to value-added chemicals offers an important route for solar-to-chemical energy conversion. However, the multi-electron and multi-pathway nature of CO_2RR makes product selectivity difficult to regulate and limits both the rational design and rapid screening of photocatalysts toward targeted products. In this work, density functional theory (DFT) calculations and machine learning (ML) were combined to investigate CO_2RR selectivity on M@N-WS_2 catalysts. Rh@N-WS_2 and Pd@N-WS_2 preferentially produce CH_3OH, whereas Ir@N-WS_2 and Pt@N-WS_2 favor CH_4 formation. Integrated crystal orbital Hamilton population (ICOHP) analysis identifies *CH_2OH as the pivotal branching intermediate and shows that its C–metal bonding strength governs product preference. A descriptor derived from the sure independence screening and sparsifying operator (SISSO) was established to predict ΔG values associated with the subsequent conversion pathways of *CH_2OH and identify the favored C_1 product, with ICOHP identified as the dominant factor governing pathway preference. This work provides atomic-level insight into product selectivity regulation in WS_2-based single-atom photocatalysts and offers a descriptor-guided strategy for rapid selectivity prediction.

Keywords: single-atom catalysts; product selectivity; density functional theory; machine learning; ICOHP

1. Introduction

Continued population growth and urban expansion are driving a steady increase in global energy demand, leading to extensive fossil fuel consumption and massive CO_2 emissions that exacerbate global environmental issues [1,2]. Carbon capture, utilization, and storage (CCUS) provides a practical

Copyright©2026 by the authors. Published by ELSP. This work is licensed under Creative Commons Attribution 4.0 International License, which permits unrestricted use, distribution, and reproduction in any medium provided the original work is properly cited.

route for lowering net carbon emissions and supporting long-term climate objectives [3]. Meanwhile, inspired by natural photosynthesis, the selective solar-driven conversion of CO_2 into useful chemicals offers a viable route toward a sustainable artificial carbon cycle [4]. However, CO_2 is chemically stable, and its reduction proceeds through complex multistep pathways. Catalytic performance is also highly sensitive to material composition and active-site structure, making both the rational design and rapid screening of catalysts toward specific products challenging. Therefore, the development of this field requires not only photocatalysts that combine high activity with high selectivity, but also interpretable methods capable of revealing structure–performance relationships and predicting product selectivity.

Ultrathin tungsten disulfide (WS_2) nanosheets have attracted growing interest in photocatalysis because of their suitable band structure for light-driven reactions [5], high carrier mobility [6,7], and relatively low preparation cost [8]. However, the activity of pristine WS_2 is constrained by two features: most reactive sites are located at the sheet edges, and the relatively inert basal surface lacks adjustable metal centers and absorbs visible light inefficiently. To address these issues, a range of modification approaches has been explored to overcome these limitations. For example, introducing boron into Pt@WS_2 systems can stabilize isolated Pt atoms and promote charge separation, thereby enhancing the photocatalytic conversion of CO_2 to methane [9]. Constructing Z-scheme CdS/WS_2 heterojunctions can improve band alignment and suppress charge recombination, leading to enhanced photocatalytic activity [10]. In addition, supporting PtM_1 single-atom alloys on WS_2 can modulate interactions with key CO_2RR intermediates and improve the predicted CO_2 photoreduction performance [11]. These studies demonstrate that the photocatalytic CO_2 reduction activity of WS_2 can be effectively enhanced through structural and electronic regulation.

However, improved catalytic activity does not necessarily lead to effective control over product selectivity. CO_2RR involves multiple proton-coupled electron-transfer steps and several competing pathways, making the resulting product distribution difficult to predict and regulate. Previous studies have shown that interactions between active sites and reaction intermediates play a central role in determining pathway preference and product selectivity [12,13]. A DFT study of M@MoS_2 catalysts identified the binding energy of *HCOO as an effective descriptor of CO_2RR activity [14]. Ethylene–ethanol selectivity on Cu is governed by how strongly oxygen-containing species interact with the surface, because this interaction determines the tendency for C–O bond cleavage [15]. Another study based on integrated crystal orbital Hamilton population (ICOHP) analysis found that stronger bonding between Cr sites and adsorbed intermediates stabilizes key species involved in the rate-determining step, thereby redirecting the subsequent reaction pathway [16]. These findings suggest that quantitative characterization of intermediate–active-site bonding is essential for understanding protonation preference, pathway divergence, and the origin of product selectivity. ICOHP analysis provides an orbital-level measure of bond strength and therefore offers a useful means of establishing quantitative relationships between bonding characteristics and product selectivity.

Although such analysis can reveal the microscopic origin of product selectivity, extending complete DFT pathway calculations and detailed bonding analyses to a broad range of candidate catalysts remains computationally demanding, making rapid screening difficult [17]. This limitation creates a need for predictive approaches that can extract transferable relationships from available computational data [18]. Machine learning (ML) provides a practical route for this purpose and has been increasingly applied

in CO_2RR studies to predict catalytic performance and identify key descriptors [19–23]. For example, one study used an ML model to relate the intrinsic properties of catalysts to their CO_2RR performance [24]. In a separate investigation, the sure independence screening and sparsifying operator (SISSO) method was applied to extract descriptors reflecting the CO_2 activation capability of M–Pt@Cu catalysts [25]. In addition, high-throughput calculations combined with SISSO have been used to screen 192 single-atom catalysts supported on 1T-phase transition-metal dichalcogenide monolayers, establishing relationships between intrinsic material properties, key reaction free energies, and product preference [26]. Among these methods, SISSO is particularly suitable for extracting physically meaningful descriptors from limited datasets [27,28]. This work focuses on CH_3OH/CH_4 pathway divergence at the common *CH_2OH intermediate on M@N-WS_2. By relating bond-specific ICOHP information to the free-energy changes of competing conversion steps and incorporating final-state adsorption energetics, we aim to provide a bonding-level interpretation of the metal-dependent thermodynamic preference between these branches.

Herein, Rh, Pd, Ir, and Pt single atoms anchored on N-doped WS_2 were selected as model catalysts to elucidate the origin of CH_4/CH_3OH selectivity and establish an interpretable framework for predicting C_1 product preference in photocatalytic CO_2 reduction. DFT was used to trace the preferred reaction routes and identify the intermediate that defines the pathway branch point. ICOHP analysis was then used to quantify intermediate–metal bonding and clarify its role in governing product preference. Building on these mechanistic insights, SISSO was employed to extract physically meaningful features, construct an interpretable ΔG_{Pred} descriptor, and establish a prediction workflow for identifying the preferred conversion pathway at the branching point and the corresponding C_1 product. By integrating reaction pathway analysis, bonding characterization, and descriptor construction, this work aims to uncover the structure–selectivity relationship of WS_2-based single-atom catalysts and provide a practical basis for their rational design and rapid screening toward targeted C_1 products.

2. Theoretical basis

Spin-polarized density functional theory (DFT) calculations were performed with the Vienna Ab initio Simulation Package (VASP) [29]. Exchange–correlation effects were treated using the Perdew-Burke-Ernzerhof (PBE) functional within the generalized gradient approximation (GGA) [30], together with projector augmented-wave (PAW) potentials for describing core–valence interactions [31]. Solvation effects during the CO_2 reduction process were considered using the VASPsol model [32,33], whereas long-range dispersion interactions were accounted for using the DFT-D3 correction [34]. A plane-wave cutoff of 500 eV and a 3 × 3 × 1 Monkhorst–Pack grid were adopted [35]. Geometry optimizations were performed until the residual atomic forces and total energy converged to 0.02 eV $Å^{-1}$ and 10^{-5} eV, respectively. Periodic interactions between neighboring slabs were minimized by introducing a 20 Å vacuum region along the z direction. Charge redistribution was evaluated through Bader analysis using the program developed by Henkelman and co-workers [36]. ICOHP values were obtained using LOBSTER to quantitatively evaluate the relevant bonding interactions [37,38].

The formation energy (E_F) of M@N-WS_2 was calculated using the following formula:

$$E_F = E_{M@N-WS2} - E_{M-bulk} - E_{N-WS2} \quad (1)$$

where $E_{M@N\text{-}WS2}$ represents the total energy of single-atom metal-modified N-doped WS_2. $E_{M\text{-}bulk}$ denotes the energy per metal atom in its bulk phase. $E_{N\text{-}WS2}$ represents the total energy of the N-doped WS_2 substrate.

The adsorption energy (E_{ads}) was calculated as:

$$E_{ads} = E_{total} - E_{substrate} - E_{adsorbate} \tag{2}$$

where E_{total}, $E_{substrate}$, and $E_{adsorbate}$ represent the total energies of the adsorption complex, the clean substrate, and the free adsorbate molecule, respectively.

The charge density difference ($\Delta\rho$) was calculated to examine charge redistribution between the adsorbate and substrate, using the following expression [39]:

$$\Delta\rho = \rho_{A-S} - \rho_A - \rho_S \tag{3}$$

where $\rho_{A\text{-}S}$, ρ_A, and ρ_S are the charge density of the adsorbate–substrate system, the adsorbate, and the substrate.

The Gibbs free energy change (ΔG) of an elementary reaction step was evaluated as:

$$\Delta G = \Delta E_{DFT} + \Delta E_{ZPE} - T\Delta S \tag{4}$$

where ΔE_{DFT}, ΔE_{ZPE} and ΔS are the electronic-energy change, zero-point-energy correction, and entropy change, respectively [40]. The temperature T is set to 298.15 K.

Proton–electron transfer steps were treated using the computational hydrogen electrode (CHE) model. At U = 0 V versus the standard hydrogen electrode (SHE), pH = 0, and an H_2 pressure of 1 bar, the chemical potential of a proton–electron pair satisfies:

$$\mu(\mathrm{H^+}) + \mu(\mathrm{e^-}) = \frac{1}{2}G(\mathrm{H_2}) \tag{5}$$

Thus, for a hydrogenation step $^*A + H^+ + e^- \rightarrow {}^*AH$, where * denotes an adsorbed species, the reaction free energy was calculated as:

$$\Delta G(^*\mathrm{A} + \mathrm{H^+} + \mathrm{e^-} \rightarrow {}^*\mathrm{AH}) = G(^*\mathrm{AH}) - G(^*\mathrm{A}) - \frac{1}{2}G(\mathrm{H_2}) \tag{6}$$

All free-energy comparisons were performed under these CHE reference conditions, without additional electrode-potential or pH corrections.

The SISSO algorithm was employed to construct explicit predictive expressions. Pairwise linear dependence among the initial features was examined using Pearson's correlation coefficient [41]:

$$p = \frac{\sum_i (x_i - \bar{x})(y_i - \bar{y})}{\sqrt{\sum_i (x_i - \bar{x})^2 \sum_i (y_i - \bar{y})^2}} \tag{7}$$

where x and y denote two evaluated descriptors. The sign of the correlation coefficient indicates the direction of their linear relationship, whereas its absolute value reflects the correlation strength.

The coefficient of determination (R^2) was used to evaluate the regression fitting quality, which is expressed as follows [42]:

$$R^2 = 1 - \frac{\sum_{i=1}^{m}(X_i - Y_i)^2}{\sum_{i=1}^{m}(\bar{Y} - Y_i)^2} \quad (8)$$

here, X_i and Y_i are the predicted and reference values, respectively; m corresponds to the total number of samples, and $\bar{Y}$ is the mean of the reference values. A higher R^2 indicates closer agreement between the predicted and reference values.

The root-mean-square error (RMSE) is calculated as [42]:

$$RMSE = \sqrt{\frac{1}{m}\sum_{i=1}^{m}(X_i - Y_i)^2} \quad (9)$$

where X_i, Y_i and m have the same meanings as defined above. RMSE characterizes the overall prediction error of the model and is sensitive to large deviations, thereby providing a quantitative measure of predictive accuracy.

3. Results

3.1. Electronic properties of WS_2

A 4 × 4 × 1 supercell was employed to construct the WS_2 catalytic model in Figure 1a. The optimized lattice parameters of WS_2 are 12.73 × 12.73 × 12.98 Å, which agree well with earlier experimental observations [43] and theoretical results [44]. Based on this model, N-doped WS_2 (N-WS_2) was constructed by substituting S atoms with N atoms. The calculated electronic structures of pristine WS_2 and N-WS_2 are shown in Figure 1b–c. Compared with pristine WS_2, N doping introduces additional electronic states near the Fermi level, which may shift the optical absorption toward longer wavelengths. The corresponding absorption spectrum is provided in Figure S1 of the supporting information.

The stable configurations of Pt@N-WS_2 and other single-atom-modified systems were further calculated (Figure 1d). The stability of the M@N-WS_2 catalysts was examined using formation energies and ab initio molecular dynamics (AIMD) simulations. All M@N-WS_2 (M = Rh, Pd, Ir, Pt) systems possess negative formation energies of −4.75, −2.86, −5.19, and −3.70 eV, respectively (Figure 1e). The thermal stability of Pt@N-WS_2 was further evaluated by AIMD at 300 K. Only small variations in the total energy and temperature were observed throughout the simulation, with no evident structural disruption. Neither bond breaking nor obvious structural rearrangement was observed upon simulation completion. These results confirm that the Pt@N-WS_2 photocatalyst can maintain its structural stability at room temperature. The other catalysts exhibit similar structural stability; their optimized configurations and AIMD results are provided in Figure S2 of the Supporting Information.

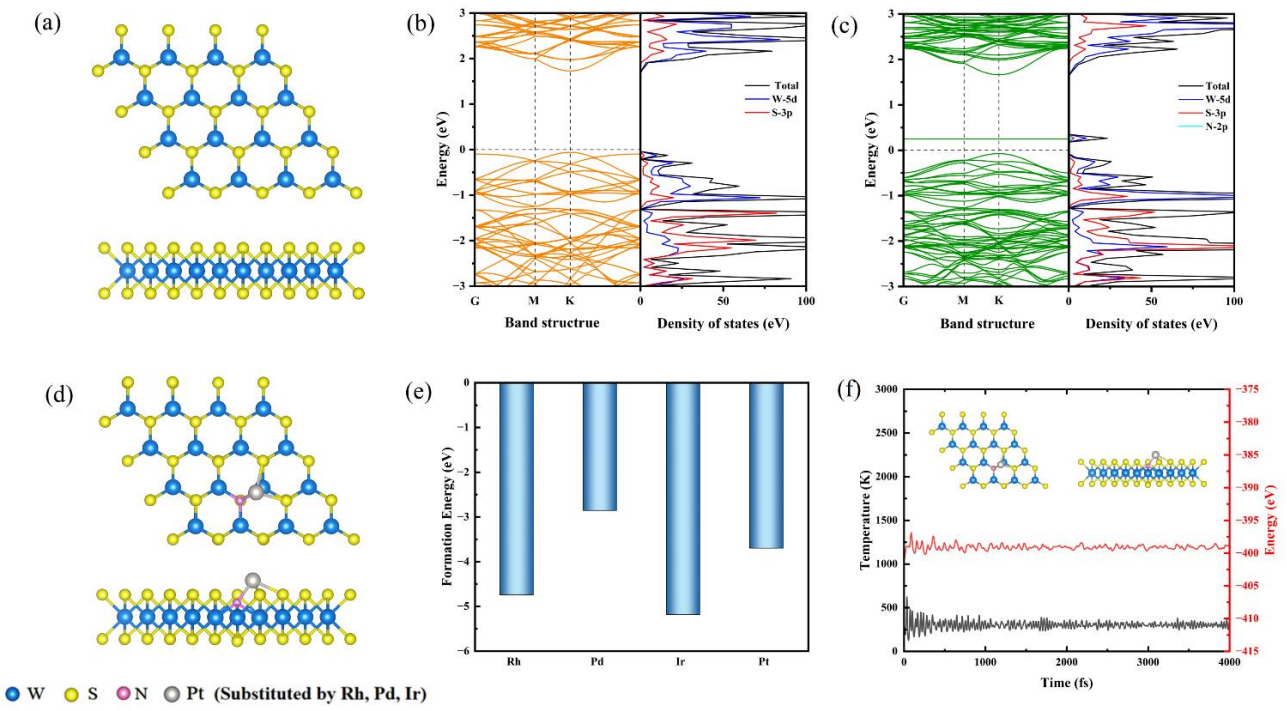


Figure 1. Atomic structures, electronic properties, and stability of WS_2-based systems. **(a)** Top and side views of the most stable WS_2 configuration; band structures and density of states of **(b)** pristine WS_2 and **(c)** N-WS_2; **(d)** Top and side views of the most stable Pt@N-WS_2 configuration; **(e)** Formation energies of M@N-WS_2 systems; **(f)** Evolution of energy (red line, right axis) and temperature (black line, left axis) during the AIMD simulation at 300 K for 4 ps with a 1 fs time step.

The electronic band structures and corresponding density of states (DOS) of M@N-WS_2 are presented in Figure 2. All M@N-WS_2 catalysts preserve a narrow-band-gap semiconducting character, although anchoring an isolated metal atom introduces additional states within the gap relative to N-WS_2. According to the DOS results, the states near the valence band maximum (VBM) primarily arise from W-5d, S-3p, and the d orbitals of the loaded metal M, whereas the conduction band minimum (CBM) mainly originates from S-3p and W-5d orbitals. The impurity states arise primarily from the hybridization between W-5d and metal-d orbitals. Notably, the pronounced overlap of S-3p, W-5d, and M-d states in the valence-band region indicates clear electronic coupling between the anchored metal atom and the N-WS_2 substrate.

The UV–vis absorption spectra of N-WS_2 and the metal-modified catalysts were compared to elucidate the influence of single-atom metal modification on the optical absorption capability of N-WS_2 (Figure 3). All M@N-WS_2 catalysts (M = Rh, Pd, Ir, and Pt) show stronger absorbance than pristine N-WS_2, especially around 500 nm, in the 600–700 nm visible-light region, and at wavelengths above 800 nm. These results indicate that single-atom metal modification can tune the optical absorption properties of N-WS_2 and boost the absorption response in the above wavelength ranges.

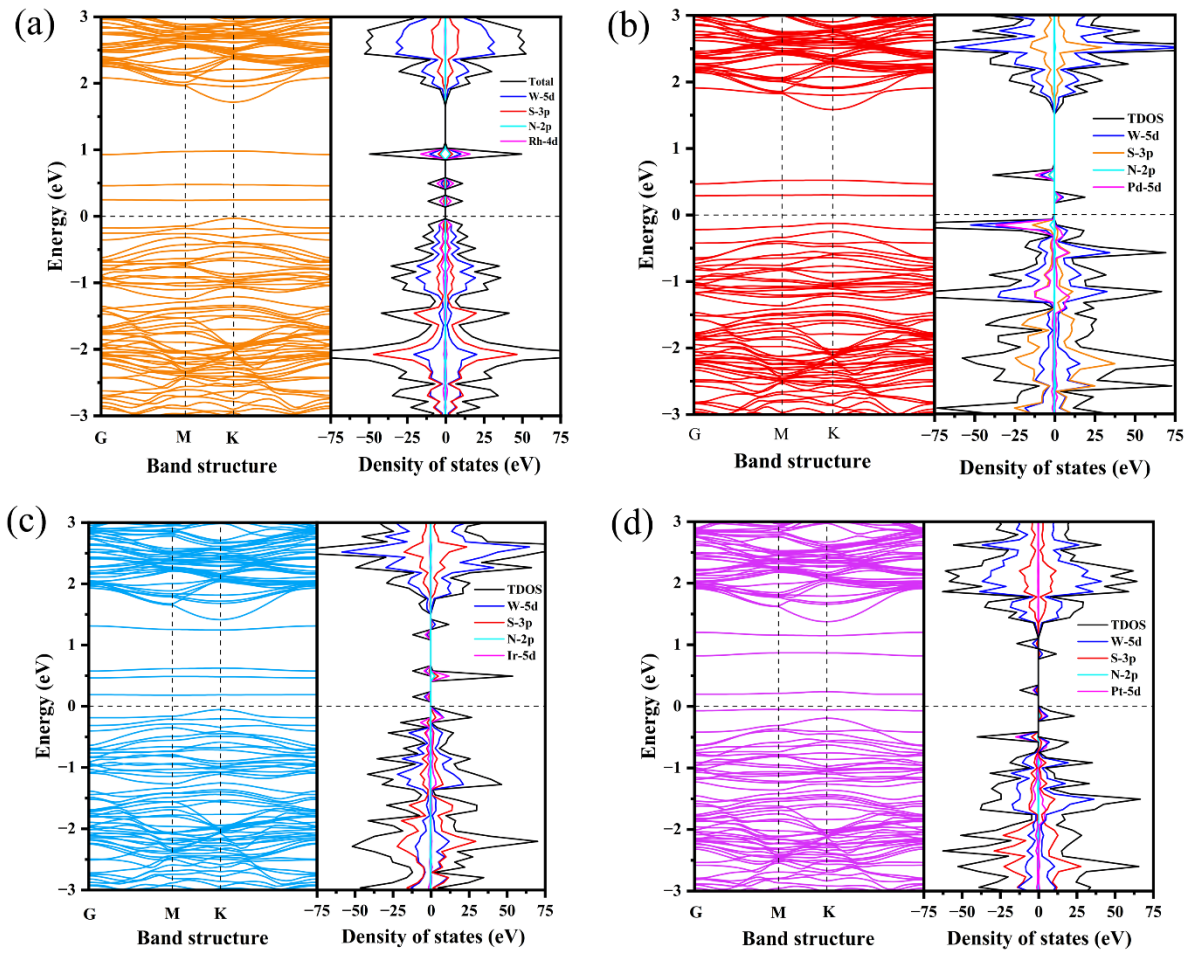


Figure 2. Band structures and corresponding density of states of **(a)** Rh@N-WS_2; **(b)** Pd@N-WS_2; **(c)** Ir@N-WS_2; and **(d)** Pt@N-WS_2.

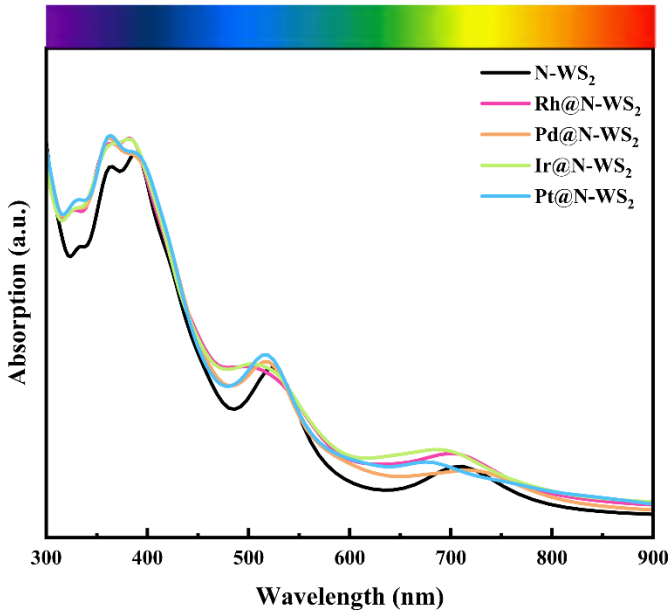


Figure 3. Calculated UV–vis absorption spectra.

3.2. Catalytic performance of M@N-WS₂

Efficient photocatalytic CO_2 reduction also relies on two prerequisites: appropriate band-edge potentials and robust CO_2 adsorption/activation on the catalyst surface [45,46]. The CBM potentials of all catalysts are more negative than the corresponding CO_2 reduction potentials, suggesting that these systems have sufficient thermodynamic driving force for CO_2RR. The band-edge positions can be found in Figure S3.

The activation degree of CO_2 is evaluated by the adsorption energy, C–O bond lengths, and O–C–O bond angle of CO_2 [47]. In general, a more negative adsorption energy, greater changes in C–O bond lengths relative to gaseous CO_2, and a smaller O–C–O bond angle indicate stronger CO_2 activation [48–50]. Based on these descriptors, the CO_2 adsorption configurations on M@N-WS_2 surfaces were examined in Figure 4. The CO_2 adsorption energies on Ir@N-WS_2 and Pt@N-WS_2 are −0.66 and −0.44 eV, respectively, more negative than those on Rh@N-WS_2 (−0.35 eV) and Pd@N-WS_2 (−0.22 eV). These results show that CO_2 can adsorb on all four catalysts, with stronger adsorption on Ir@N-WS_2 and Pt@N-WS_2. In addition, the adsorbed CO_2 molecules show clear changes in C–O bond lengths and O–C–O bond angles compared with gaseous CO_2 (1.16/1.16 Å, 180°). Larger structural distortions are observed on Ir@N-WS_2 (1.25/1.21 Å, 150.6°) and Pt@N-WS_2 (1.25/1.21 Å, 149.5°), indicating their stronger ability to activate CO_2.

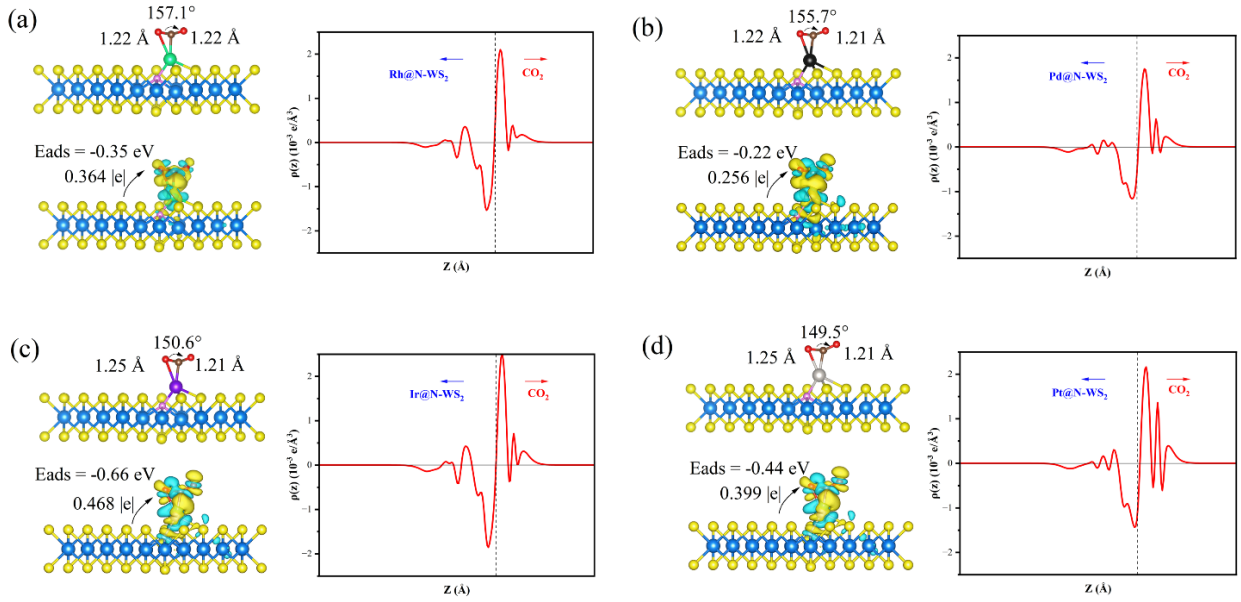


Figure 4. Side views, charge density difference plots, and planar-averaged charge density difference profiles along the c axis for the most stable CO_2 adsorption configurations on **(a)** Rh@N-WS_2; **(b)** Pd@N-WS_2; **(c)** Ir@N-WS_2; **(d)** Pt@N-WS_2. Blue and yellow indicate charge depletion and charge accumulation, respectively. The isosurface value is set to 0.002 e/Å^3.

Furthermore, CO_2 adsorption induces charge redistribution, with the adsorbed molecule accepting electrons from the catalyst. The calculated charge transfer amounts are 0.468 |e| for Ir@N-WS_2, 0.399 |e| for Pt@N-WS_2, 0.364 |e| for Rh@N-WS_2, and 0.256 |e| for Pd@N-WS_2. Together with the adsorption energies and structural distortions, the charge-transfer results indicate that Ir@N-WS_2 and Pt@N-WS_2 have stronger CO_2 adsorption and activation capabilities than Rh@N-WS_2 and Pd@N-WS_2.

The ΔG of key reaction intermediates on M@N-WS_2 were calculated to identify the preferred CO_2RR pathways and evaluate catalytic activity (Figure 5). During the initial hydrogenation of adsorbed CO_2, *COOH formation is thermodynamically favored over *HCOO formation on all four catalysts. Taking Rh@N-WS_2 as an example, *COOH formation shows a favorable ΔG of −0.17 eV, 0.21 eV lower than that of *HCOO. The ΔG values for $*CO_2 + H^+ + e^- \rightarrow$ *COOH on Ir@N-WS_2 (−0.51 eV) and Pt@N-WS_2 (−0.44 eV) are lower than those on Rh@N-WS_2 (−0.17 eV) and Pd@N-WS_2 (−0.02 eV), indicating more favorable thermodynamics for the initial CO_2 hydrogenation on Ir@N-WS_2 and Pt@N-WS_2. This trend agrees with their stronger CO_2 activation ability.

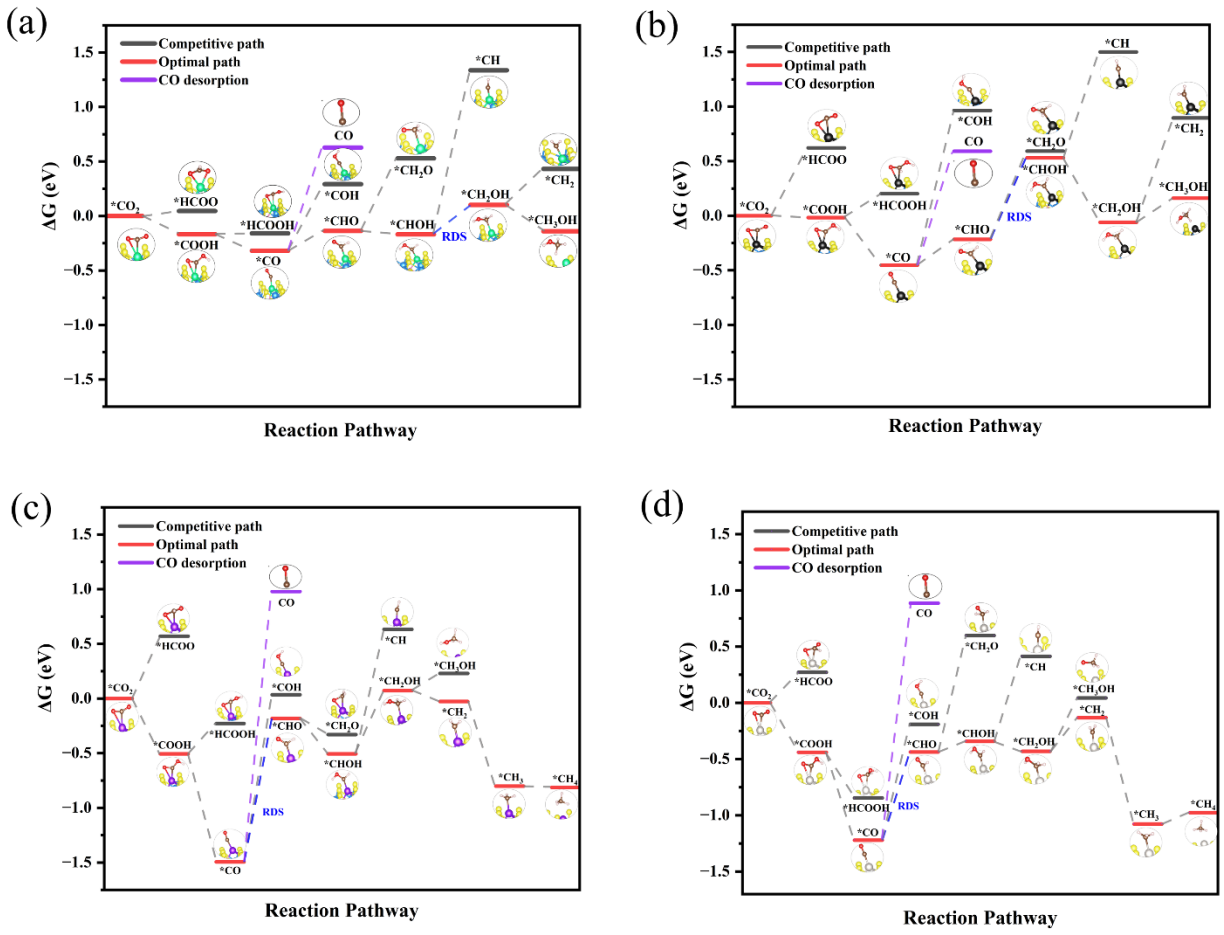


Figure 5. Reaction pathways for CO_2 reduction to CH_3OH/CH_4 on **(a)** Rh@N-WS_2; **(b)** Pd@N-WS_2; **(c)** Ir@N-WS_2; **(d)** Pt@N-WS_2.

The subsequent hydrogenation pathway on Rh@N-WS_2 is shown in Figure 5a. In the second hydrogenation step, *COOH is converted to *CO with a ΔG of −0.15 eV, which is more favorable than the competing formation of *HCOOH (0.01 eV). For the third hydrogenation step, *CO can undergo further hydrogenation to form *CHO or *COH, or desorb as gas-phase CO. The Gibbs free energy change for *CHO formation is 0.18 eV, lower than those for *COH formation (0.61 eV) and CO desorption (0.95 eV), indicating that *CHO formation is thermodynamically preferred under the adopted reference conditions. The same preference is also observed for the other three catalysts. The calculated *CO adsorption energy reflects the competition between *CO desorption and its subsequent hydrogenation [51]. A negative correlation between *CO adsorption energy and ΔG(*CO + H^+ +

e⁻→*CHO) is plotted in Figure 6a. Rh@N-WS_2 shows an *CO adsorption energy of −1.68 eV, together with a low Δ*G* of 0.18 eV for *CHO formation. This moderate *CO binding helps avoid premature *CO desorption while allowing further hydrogenation toward deeply reduced products.

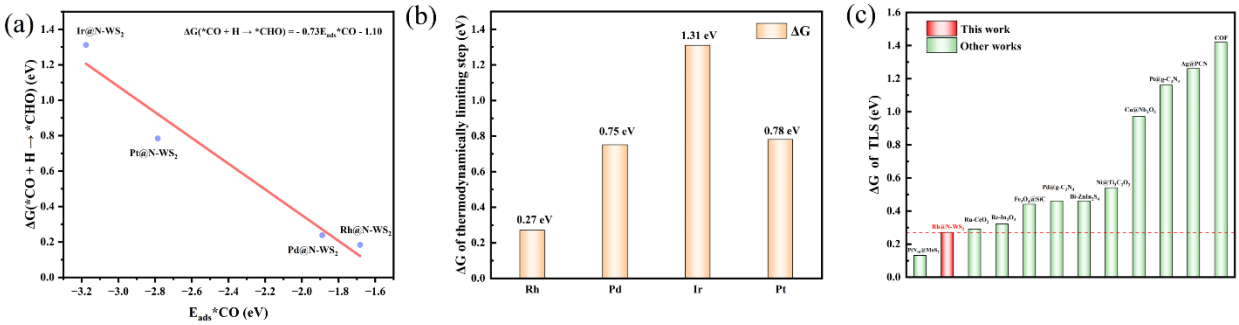


Figure 6. CO adsorption and CO_2 reduction energetics of M@N-WS_2 catalysts. **(a)** Relationship between the *CO adsorption energy and Δ*G*(*CO + H^+ + e^- → *CHO); **(b)** Gibbs free-energy changes of the thermodynamically limiting steps on M@N-WS_2; **(c)** Comparison of the corresponding value for Rh@N-WS_2 with DFT values reported for other catalysts [52–56]. The literature comparison is qualitative because computational methods and reference conditions differ among studies.

The fourth hydrogenation converts *CHO to *CHOH with a ΔG of −0.03 eV, which is thermodynamically more favorable than the competing formation of *CH_2O (ΔG = 0.67 eV). In the fifth elementary step, *CHOH is hydrogenated to *CH_2OH with a Δ*G* of 0.27 eV, which is much lower than that for the formation of the *CH intermediate (1.50 eV). The final hydrogenation of *CH_2OH preferentially yields *CH_3OH with a Δ*G* of −0.24 eV, rather than forming *CH_2 (0.33 eV). Therefore, the preferred CO_2 reduction pathway on Rh@N-WS_2 is *CO_2 → *COOH → *CO → *CHO → *CHOH → *CH_2OH → *CH_3OH → CH_3OH.

The same analysis was then applied to the other metal-modified catalysts. Pd@N-WS_2 follows a pathway similar to that of Rh@N-WS_2, leading to CH_3OH as the final product. In contrast, Ir@N-WS_2 and Pt@N-WS_2 favor a different route: *CO_2 → *COOH → *CO → *CHO → *CHOH → *CH_2OH → *CH_2 → *CH_3 → *CH_4, which eventually produces CH_4. The ΔG values of all elementary steps are summarized in Table S1 of the Supporting Information.

To compare the catalytic activities of the four catalysts, the thermodynamically limiting step (TLS), defined as the elementary step with the largest positive Δ*G* in CO_2RR, was identified for each system (Figure 6b). Rh@N-WS_2 shows the lowest TLS free energy change of 0.27 eV, indicating the most favorable reaction thermodynamics among the four catalysts. Furthermore, this value is lower than most of the previously reported DFT values (Figure 6c) [52–56], suggesting favorable CO_2RR thermodynamics. Given possible discrepancies in computational methods and reference conditions across studies, this comparison is only qualitative. In addition to activity differences, the four catalysts display clear metal-dependent product selectivity. Rh@N-WS_2 and Pd@N-WS_2 preferentially yield CH_3OH, whereas Ir@N-WS_2 and Pt@N-WS_2 favor CH_4 as the major C_1 product. This study focuses on the relative thermodynamic preference between the investigated CH_3OH- and CH_4-forming CO_2 reduction pathways. CO desorption was included in the pathway analysis, whereas the competing hydrogen evolution reaction (HER) was not explicitly evaluated. Accordingly, the CH_3OH/CH_4

preferences reported here are confined to the examined CO_2RR pathways and do not establish the overall product selectivity under aqueous photocatalytic conditions.

3.3. Mechanistic analysis of product selectivity

Further analysis of the CO_2 photoreduction pathways on M@N-WS_2 revealed the origin of the observed selectivity differences. Although the four M@N-WS_2 catalysts follow an identical reaction pathway before *CH_2OH formation, their subsequent conversion differs markedly. On the Rh- and Pd-modified catalysts, *CH_2OH preferentially proceeds toward *CH_3OH, whereas on the Ir- and Pt-modified catalysts, it is converted to *CH_2 and ultimately yields CH_4 in Figure 7a. Therefore, the subsequent conversion of *CH_2OH determines the selectivity between CH_3OH and CH_4.

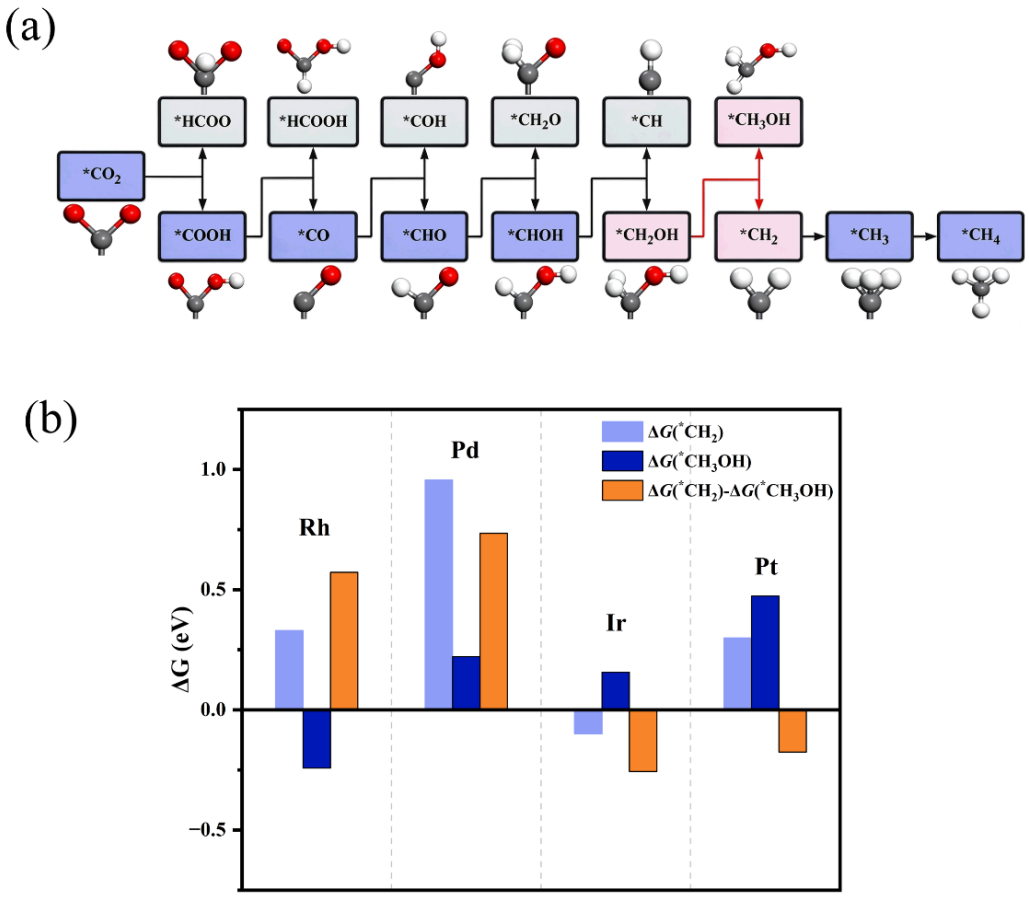


Figure 7. CO_2 reduction pathways and thermodynamic analysis of C_1 product formation. **(a)** Main CO_2 reduction pathways leading to C_1 products; **(b)** Values of ΔG(*CH_2) – ΔG(*CH_3OH) for Rh@N-WS_2, Pd@N-WS_2, Ir@N-WS_2, and Pt@N-WS_2.

To reveal the origin of this pathway divergence, the ΔG values for the conversion of *CH_2OH to *CH_2 (ΔG(*CH_2)) and *CH_3OH (ΔG(*CH_3OH)) were adopted to quantitatively evaluate the relative favorability of the two reduction pathways (Figure 7b). In the M@N-WS_2 systems, Rh@N-WS_2 gave a positive value of ΔG(*CH_2) – ΔG(*CH_3OH) (0.57 eV), while Pd@N-WS_2 also presented a positive value of 0.73 eV. Both catalysts preferentially converted *CH_2OH into *CH_3OH. By

contrast, Ir@N-WS_2 and Pt@N-WS_2 show negative values of −0.26 and −0.18 eV, respectively, indicating that *CH_2 formation is thermodynamically preferred and the reaction eventually proceeds toward CH_4. Thus, the sign of ΔG(*CH_2) – ΔG(*CH_3OH) indicates the thermodynamically preferred branch within the examined pathways: positive values favor CH_3OH formation, whereas negative values favor CH_4 formation.

The charge density difference analysis was performed for the adsorbed *CH_2OH intermediate on the four metal active sites (Figure 8a–d). The charge density difference maps show electron accumulation near both the C and O atoms of *CH_2OH, suggesting two possible subsequent pathways: hydrogen addition at the C atom to form *CH_3OH, or hydrogen addition at the O atom accompanied by H_2O desorption to generate *CH_2. In addition, the charge transfer between *CH_2OH and Ir@N-WS_2/Pt@N-WS_2 is 0.19 |e| and 0.23 |e|, respectively, higher than that in Rh@N-WS_2 (0.12 |e|) and Pd@N-WS_2 (0.10 |e|). This more pronounced interfacial charge redistribution suggests stronger electronic coupling between *CH_2OH and the Ir/Pt active sites, which may affect the preferred hydrogenation site in the subsequent reaction.

Given the important role of active site–intermediate interactions in determining CO_2 reduction selectivity [57–59], we further examined the adsorption strength of *CH_2OH and the corresponding C–M bond length, where C is the carbon atom of *CH_2OH and M is the metal active site (Figure 8e–h). Compared with Rh@N-WS_2 and Pd@N-WS_2, Ir@N-WS_2 and Pt@N-WS_2 show more negative *CH_2OH adsorption energies of −2.91 and −3.32 eV, respectively, with C–M bond lengths of 2.01 Å and 1.96 Å. In contrast, Rh@N-WS_2 and Pd@N-WS_2 show adsorption energies of −2.46 and −2.67 eV, respectively, with similar C–M bond lengths of 2.02 Å. These results indicate stronger C–M interactions in the Ir- and Pt-modified systems. Carbon-site hydrogenation followed by methanol desorption ultimately requires cleavage of the C–M coordination. In contrast, oxygen-site hydrogenation followed by C–O bond cleavage and H_2O release produces *CH_2 while retaining the C–M coordination. Stronger C–M bonding is therefore consistent with a preference for the *CH_2-formation branch, which retains this coordination, whereas relatively weaker C–M bonding is consistent with the methanol-formation branch, which ultimately requires its cleavage. Thus, the relatively weaker C–M interactions on Rh@N-WS_2 and Pd@N-WS_2 facilitate C-site hydrogenation of *CH_2OH, thereby favoring *CH_3OH formation and ultimately methanol production.

To provide a more quantitative evaluation of the C–M bonding strength, ICOHP analysis was carried out for the adsorbed *CH_2OH intermediate (Figure 8i–l). Rh@N-WS_2 and Pd@N-WS_2 show less negative ICOHP values of −2.86 eV and −2.72 eV, respectively, indicating weaker C–M bonding. In comparison, Ir@N-WS_2 and Pt@N-WS_2 have more negative ICOHP values of −3.17 eV and −3.46 eV, respectively, corresponding to stronger C–M interactions. Consistent with the projected orbital-overlap results shown in Figure S4, these ICOHP results further confirm that the different C–M bonding interactions between *CH_2OH and metal active sites are a key factor governing the product selectivity of M@N–WS_2 catalysts.

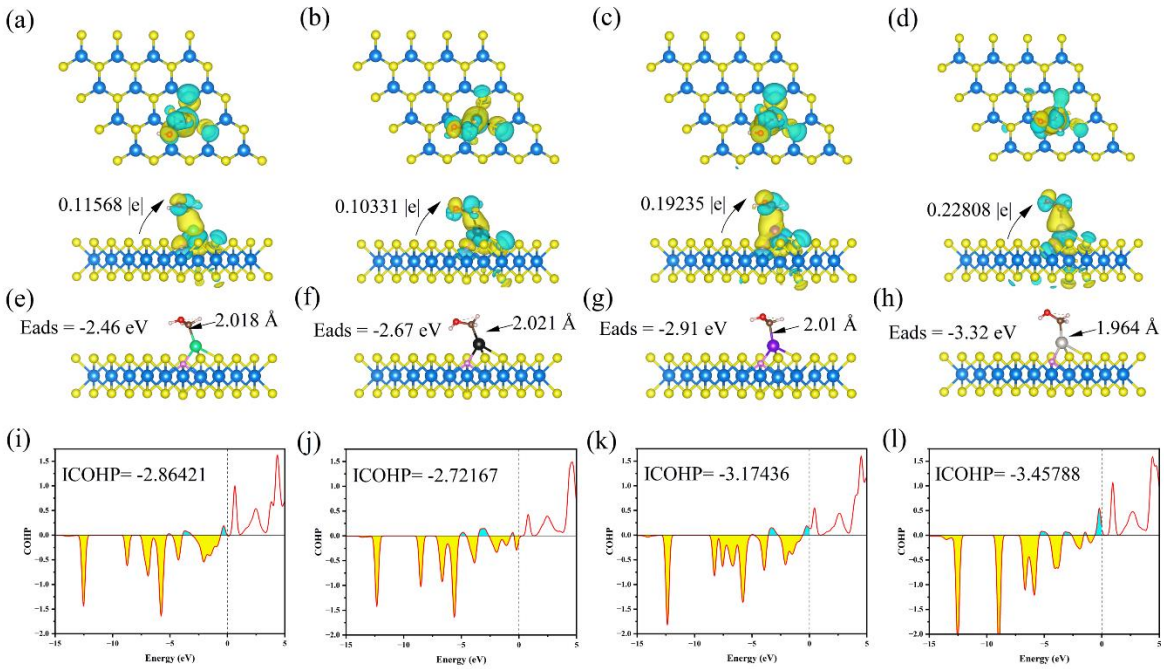


Figure 8. Charge density difference plots for *CH_2OH adsorption on **(a)** Rh@N-WS_2; **(b)** Pd@N-WS_2; **(c)** Ir@N-WS_2; **(d)** Pt@N-WS_2. Blue and yellow indicate charge depletion and charge accumulation, respectively, with an isosurface value of 0.002 e/Å^3. The most stable *CH_2OH adsorption configurations and corresponding adsorption energies on **(e)** Rh@N-WS_2; **(f)** Pd@N-WS_2; **(g)** Ir@N-WS_2; **(h)** Pt@N-WS_2. COHP profiles of the C–M bond in adsorbed *CH_2OH on **(i)** Rh@N-WS_2; **(j)** Pd@N-WS_2; **(k)** Ir@N-WS_2; and **(l)** Pt@N-WS_2. The dashed line denotes the Fermi level.

To further examine the kinetic preference between the two competing branches, transition-states calculations were performed for *CH_2OH hydrogenation toward CH_3OH or toward *CH_2 accompanied by H_2O release (Figure S5). On Rh@N-WS_2 and Pd@N-WS_2, the calculated activation energies for CH_3OH formation are 0.63 and 0.50 eV, respectively, substantially lower than those for the competing *CH_2-forming steps (4.62 and 3.19 eV). Conversely, Ir@N-WS_2 and Pt@N-WS_2 exhibit lower activation energies for *CH_2 formation (1.45 and 1.56 eV, respectively) than for CH_3OH formation (3.56 and 3.54 eV). The barrier ordering is therefore consistent with the thermodynamic branch preferences identified above, providing complementary kinetic support for CH_3OH formation on Rh/Pd and the *CH_2 branch leading toward CH_4 on Ir/Pt within the modeled surface hydrogenation pathways.

3.4. Descriptor construction for quantitative prediction of product selectivity

To establish a quantitative relationship between bonding characteristics and pathway preference, SISSO was used to construct an interpretable model for predicting reaction free-energy changes. Here, ΔG denotes the Gibbs free energy change of an individual elementary reaction step, defined as the free-energy difference between its final and initial states. The SISSO workflow contains four main steps: (i) constructing the initial dataset from DFT calculations; (ii) screening relevant primary features using Pearson correlation analysis; (iii) generating and selecting descriptors; and (iv) evaluating the generalization capability.

To improve the reliability of the prediction model, the initial features were selected from three aspects: (i) properties of the metal active site, (ii) structural features of the catalyst, and (iii) properties of surface reaction intermediates. Based on this strategy, eleven candidate features were first collected, with the corresponding data compiled in Table S2 of the supporting information. These features cover the main physicochemical factors that may affect catalytic performance. Because an excessive number of redundant input features may increase model complexity and weaken its generalization ability, Pearson correlation coefficients (p) were calculated to examine the pairwise linear correlations between the primary features [60–63]. Feature pairs with $|p| > 0.80$ were regarded as strongly correlated, and only one feature from each strongly correlated pair was retained to reduce redundancy. For example, ε_d was strongly correlated with r_{m_X}, while IE_1 showed strong correlations with both Z_X and M_X within the candidate feature set used for ΔG prediction in Figure S6 of the supporting information. Accordingly, only ε_d and IE_1 were retained from these correlated features. Finally, eight representative primary features were selected, as summarized in Table 1. These structural and electronic features have also been used in previous theoretical and experimental studies, supporting their physical relevance for describing catalyst–intermediate interactions and product selectivity [20,24,64].

Table 1. Summary of the selected features, classified into three categories: metal-site-related, catalyst-related, and intermediate-related features.

Category	Name	Abbreviation
Metal-site-related features	d-electron number of X	N_d
	Electronegativity	χ_X
	First ionization energy	IE_1
Catalyst-related features	d-band center	ε_d
	Work function	σ
Intermediate-related features	Adsorption energy of initial-state intermediate	E_{adsIS}
	Adsorption energy of final-state intermediate	E_{adsFS}
	Integrated crystal orbital Hamilton population	ICOHP

The DFT-calculated ΔG values were used as targets, and the selected primary features were used as model inputs. The dataset comprises 24 catalyst–reaction pairs, with six samples from each of the Rh-, Pd-, Ir-, and Pt-modified systems. Samples M1–M6 correspond to the six consecutive elementary steps along $*CO_2 \rightarrow *COOH \rightarrow *CO \rightarrow *CHO \rightarrow *CHOH \rightarrow *CH_2OH \rightarrow *CH_3OH/*CH_2$, where M denotes the metal center. Specifically, the four samples corresponding to the hydrogenation of $*CH_2OH$—Rh6, Pd6, Ir6, and Pt6—were reserved as a test set. These samples represent $*CH_2OH + H^+ + e^- \rightarrow *CH_3OH$ on the Rh- and Pd-modified catalysts and $*CH_2OH + H^+ + e^- \rightarrow *CH_2 + H_2O$ on the Ir- and Pt-modified catalysts. The remaining 20 samples were used for SISSO descriptor identification and coefficient fitting. This partition aims to test whether the descriptor trained on the preceding elementary steps can predict the free-energy change of the $*CH_2OH$ hydrogenation step that governs product selectivity. The elementary operators used for feature-space construction are listed in

Table S3. The numerical values of all primary features and the corresponding DFT-calculated ΔG targets for the 24 samples are provided in Tables S4–S7. Notably, adsorption energies describe the overall energetic changes associated with adsorbate–surface binding, whereas ICOHP characterizes the contribution of a specified metal–intermediate contact to the occupied band-structure energy. ICOHP therefore provides bond-specific electronic information that is not explicitly resolved by the overall adsorption energy. The resulting two-dimensional SISSO model is expressed as follows:

$$\Delta G_{\mathrm{Pred}} = -3.58\left(\frac{(\sigma + ICOHP) \times ICOHP^2}{{N_d}^2}\right) + 0.15\left(\frac{\varepsilon_d}{|E_{ads}FS^2 - \varepsilon_d \times ICOHP|}\right) + 0.953 \quad (10)$$

Equation (10) reproduces the DFT-calculated ΔG values of the 20 training samples with an R^2 of 0.953 and an RMSE of 0.11 eV, indicating a close fit to the training data. For the four test samples, the descriptor yields an R^2 of 0.937 and an RMSE of 0.14 eV (Figure 9a). The agreement between the predicted and DFT-calculated values on the test set supports the predictive capability of the descriptor within the investigated catalyst systems. The descriptor comprises two composite components:

$$d_1 = \left(\frac{(\sigma + ICOHP) \times ICOHP^2}{{N_d}^2}\right)$$

$$d_2 = \left(\frac{\varepsilon_d}{|E_{ads}FS^2 - \varepsilon_d \times ICOHP|}\right)$$

Equation (10) combines bonding and electronic information through two composite components. The first, d_1, captures the coupling between local bonding in the initial state and the catalyst's electronic environment, relating metal–intermediate interactions to reaction energetics. The second, d_2, couples final-state adsorption energetics with the initial bonding and electronic environment, distinguishing the energetic consequences of different final states. Together, they connect the bonding environment of the initial intermediate with the adsorption characteristics of the reaction products. For the two branches on a given catalyst, the initial-state ICOHP and catalyst properties are identical, so d_1 cancels when comparing their predicted ΔG values. Their different final-state adsorption energies lead to different d_2 values and consequently different predicted ΔG values, distinguishing the thermodynamically preferred pathway. For the same elementary reaction, such as *CH_2OH hydrogenation, on different catalysts, differences in ICOHP reflect metal-dependent C–M bonding interactions. ICOHP enters d_1 through a cubic term, contributing to the predicted reaction free energy. The schematic in Figure S7 illustrates a possible nonlinear dependence, qualitatively consistent with the Sabatier principle [65]: an appropriate interaction strength is required, whereas interactions that are either too weak or too strong shift ΔG toward more positive values, making the reaction thermodynamically less favorable. Therefore, differences in the strength of metal–intermediate interactions determine the product selectivity of different catalysts.

Furthermore, four-fold leave-one-metal-out cross-validation [66] was performed to evaluate predictive performance across different metal centers (Figure 9b). The 24 samples were divided into four groups according to metal identity, with six samples associated with each of the Rh-, Pd-, Ir-, and Pt-modified systems. In each iteration, all six samples from one metal system were used as the test set, while the remaining 18 samples were used for SISSO descriptor identification and coefficient fitting.

Consequently, samples from the same metal system were never present in both the training and test sets within a given iteration. The sample assignments are provided in Table S8, and predictive performance was evaluated using the R^2 and RMSE of the test sets. The corresponding descriptor expressions are given in Equations (11)–(14).

$$\Delta G_{\mathrm{Pred}} = 3.15\left(\frac{(\sigma + ICOHP) \times ICOHP^3}{{N_d}^3}\right) + 0.014\left(\frac{\sigma + E_{adsFS}}{|E_{adsIS} + \sigma + \varepsilon_d|}\right) + 0.450 \quad (11)$$

$$\Delta G_{\mathrm{Pred}} = -1.03\left(\frac{N_d}{ICOHP^2 + IE_1 + ICOHP}\right) + 0.01\left(\frac{(E_{adsFS} - \varepsilon_d)^2}{E_{adsIS} - ICOHP}\right) - 1.17 \quad (12)$$

$$\Delta G_{\mathrm{Pred}} = 4.55\left(\frac{(\sigma + ICOHP) \times ICOHP^3}{{N_d}^3}\right) + 0.94\left(|\varepsilon_d - E_{adsIS}| - \frac{\varepsilon_d * E_{adsFS}}{\sigma}\right) - 0.526 \quad (13)$$

$$\Delta G_{\mathrm{Pred}} = 2.98\left(\frac{(\sigma + ICOHP) \times ICOHP^3}{{N_d}^3}\right) + 0.0001\left(\frac{ICOHP * N_d * E_{adsIS}}{IE_1}\right)^3 + 0.242 \quad (14)$$

The training and test R^2 and RMSE values for each fold are summarized in Table 2, and the comparisons between predicted and DFT-calculated ΔG are provided in Figure S8. As shown, the test-set R^2 values range from 0.862 to 0.963, with RMSE values of 0.165–0.238 eV. The predicted ΔG values agree reasonably well with the DFT results for the metal systems. The favorable predictive performance across all folds demonstrates the cross-metal predictive capability of the SISSO modeling procedure within the investigated systems.

Table 2. Training and test performance of the SISSO models in leave-one-metal-out cross-validation.

CV	Training R^2	Training RMSE (eV)	Test R^2	Test RMSE (eV)
CV_1	0.917	0.159	0.921	0.191
CV_2	0.973	0.052	0.963	0.165
CV_3	0.971	0.093	0.913	0.203
CV_4	0.818	0.241	0.862	0.238

To quantify the predictive contribution of each feature, a feature-ablation analysis was performed by removing one feature at a time and repeating SISSO descriptor identification and coefficient fitting within each training fold. The full and ablated models used identical cross-validation partitions, descriptor dimensionality, and feature-construction settings. Feature contributions were evaluated using the change in test-set RMSE, defined as:

$$\Delta RMSE_{\mathrm{j,i}} = RMSE_{without\ j,i} - RMSE_{full,i} \quad (15)$$

where j denotes the removed feature and i denotes the cross-validation fold. Among the examined features, removing ICOHP produced the largest increase in test-set RMSE (Table S9). ICOHP therefore exhibited the largest predictive contribution under the adopted ablation criterion. Together with the preceding bonding analysis, these results support ICOHP as an important bonding descriptor for characterizing reaction free-energy changes, which in turn gives rise to differences in product selectivity. Similar interaction-regulated selectivity behavior has also been reported in several catalytic systems, including $Cs_2AgBiBr_6$/BiOBr S-scheme heterojunctions [67], oxide-derived Cu catalysts [68], and In_2O_3/TiO_2 S-Scheme Heterojunction [69], supporting the physical relevance of the proposed descriptor.

Based on the final SISSO expression in Equation (10), a DFT-informed workflow was established to efficiently estimate the thermodynamically preferred C_1 product of related M@N-WS_2 systems (Figure 9c). Application to a new catalyst requires optimization of the catalyst and relevant adsorbed configurations, calculation of the work function, d-band center, and final-state adsorption energies, and LOBSTER analysis to obtain the specified metal–intermediate ICOHP values. The d-electron count is assigned consistently with the training dataset. These inputs are used to predict the reaction free-energy changes for the competing conversions of *CH_2OH, denoted by ΔG(*CH_2) and ΔG(*CH_3OH). The product selectivity is then determined from the difference between ΔG(*CH_2) and ΔG(*CH_3OH). When ΔG(*CH_2) – ΔG(*CH_3OH) > 0, hydrogenation of *CH_2OH toward *CH_3OH is favored, leading to CH_3OH formation. Conversely, when this value is below zero, *CH_2 formation is preferred, and favoring the subsequent pathway toward CH_4 formation

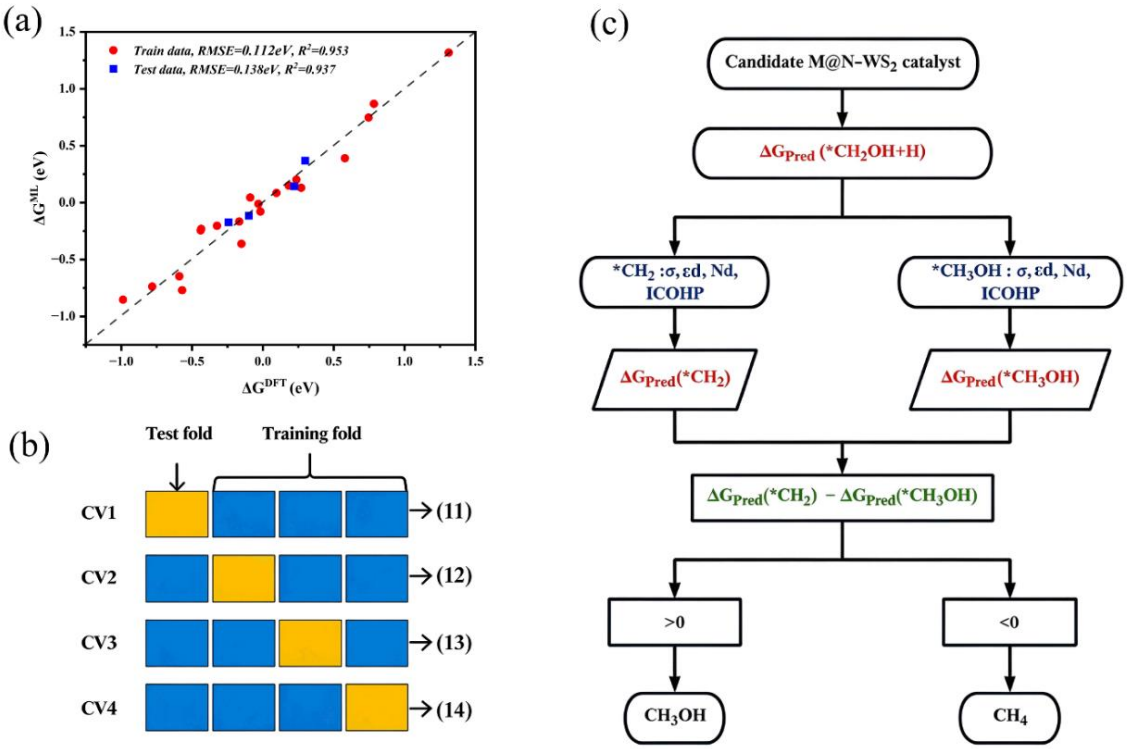


Figure 9. Performance evaluation and application of the SISSO-derived predictive model for CO_2RR selectivity screening. **(a)** Comparison of DFT-calculated and SISSO-predicted ΔG values for the training and test sets; **(b)** Leave-one-metal-out cross-validation scheme, where CV_i (i = 1 – 4) denotes a fold with one metal system held out as the test set; **(c)** Screening workflow for CO_2RR selectivity on M@N-WS_2 based on the proposed descriptor ΔG_{Pred}.

4. Conclusion

This work elucidates the origin of C_1 product selectivity in photocatalytic CO_2 reduction on M@N-WS_2 single-atom catalysts. Rh@N-WS_2 and Pd@N-WS_2 preferentially form CH_3OH, whereas Ir@N-WS_2 and Pt@N-WS_2 favor CH_4 production. The selectivity divergence occurs at the *CH_2OH intermediate and is governed by its C–metal bonding strength. ICOHP analysis shows that weaker bonding on Rh and Pd facilitates conversion toward *CH_3OH, while stronger bonding on Ir and Pt stabilizes *CH_2OH and promotes the *CH_2 pathway toward CH_4. The dominant contribution of the ICOHP to the SISSO-derived ΔG_{Pred} descriptor further demonstrates the close connection between intermediate bonding and reaction energetics. Based on this descriptor, a prediction workflow was established to identify the preferred pathway and corresponding C_1 product without evaluating every elementary step of the complete CO_2RR process. These results suggest that the bonding characteristics of key branching intermediates may serve as transferable, physically meaningful features for the preliminary prediction and rational regulation of product selectivity in related single-atom catalytic systems.

Data availability statement

The data reported in this study are available in the article and the accompanying Supporting Information. The supplementary file contains the calculated Gibbs free-energy changes for the CO_2 reduction pathways, the input feature values used for SISSO modeling, and the results of the feature ablation analysis.

Declaration of generative AI and AI-assisted technologies

The authors did not use generative AI or AI-assisted technologies in the writing of this manuscript.

Acknowledgments

This work was funded by the National Natural Science Foundation of China (22473114, U23B2087, 12104513), and the Shandong Provincial Natural Science Foundation of China (ZR2025MS247, ZR2023MB034).

Authors' contribution

Conceptualization, T.L., Y.Y. and Y.C.; methodology, H.R. and H.Z.; software, W.Z. and W.G.; validation, H.R., W.G. and H.Z.; formal analysis, Y.Y. and Y.L.; investigation, T.L.; resources, Y.C.; data curation, T.L.; writing—original draft preparation, T.L.; writing—review and editing, Y.C.; visualization, T.L. and Y.C.; supervision, Y.C. and W.G.; project administration, W.Z., H.R., H.Z. and Y.L.; funding acquisition, Y.L. and Y.C. All authors have read and agreed to the published version of the manuscript.

Conflicts of interest

The authors declare that they have no known competing financial interests or personal relationships that could have appeared to influence the work reported in this paper.

References

[1] Abdelkareem MA, Elsaid K, Wilberforce T, Kamil M, Sayed ET, *et al*. Environmental aspects of fuel cells: a review. *Sci. Total Environ.* 2021, 752:141803.

[2] Allangawi A, Alzaimoor EFH, Shanaah HH, Mohammed HA, Saqer H, *et al*. Carbon capture materials in post-combustion: Adsorption and absorption-based processes. *C* 2023, 9(1):17.

[3] Geweda AE, Zayed ME, Khan MY, Alquaity ABS. Mitigating CO_2 emissions: a review on emerging technologies/strategies for CO_2 capture. *J. Energy Inst.* 2025, 118:101911.

[4] Xu Z, Bian Z. Photocatalytic methane conversion. *Acta Phys.-Chim. Sin.* 2020, 36(3):1907013.

[5] Jin Z, Liu H, Huang T, Chen L, Tan CL, *et al*. 2D WS_2 monolayer preparation method and research progress in the field of optoelectronics. *Nanotechnology* 2025, 36(14):142002.

[6] Chen D, Tang J, Zhang X, Wu P, Li Y, *et al*. WS2 nanostructure-based gas sensor for SF6 decomposition products: experimental and first-principles study. *IEEE Sens. J.* 2022, 22(21):20171–20176.

[7] Radomski P, Szary MJ. Transition metals *vs*. chalcogens: the impact on NOx adsorption on MoS2, MoSe2 and WS2 transition-metal dichalcogenides. *Acta Mater.* 2024, 272:119949.

[8] Song JG, Park J, Lee W, Choi T, Jung H, *et al*. Layer-controlled, wafer-scale, and conformal synthesis of tungsten disulfide nanosheets using atomic layer deposition. *ACS Nano* 2013, 7(12):11333–11340.

[9] Zhu L, Qin C, Wang Y, Cao J. Single-atom Pt supported on non-metal doped WS2 for photocatalytic CO_2 reduction: a first-principles study. *Appl. Surf. Sci.* 2023, 626:157252.

[10] Wang G, Dou K, Cao H, Du R, Liu J, *et al*. Designing Z-scheme CdS/WS_2 heterojunctions with enhanced photocatalytic degradation of organic dyes and photoreduction of Cr(VI): experiments, DFT calculations and mechanism. *Sep. Purif. Technol.* 2022, 291:120976.

[11] Zhu L, Qin C, Wang Y, Cao J. Photocatalytic CO_2 reduction to CH_4 over PtM1 single-atom alloys modified WS2: A first-principles study. *Mol. Catal.* 2024, 554:113815.

[12] Si F, Bai J, Li Y, Lan R, Cheng S, *et al*. Regulating reactive oxygen species via orbital rehybridization between intermediate and active site for selective methane photooxidation to methanol. *Angew. Chem. Int. Ed.* 2025, 64(30):e202505267.

[13] Sun L, Liu Y, Du S, Wang C, Guo H, *et al*. Investigation of heat treatment medium for C_2^+ alcohols synthesis from syngas over binary CuZn catalyst. *Int. J. Hydrogen Energy* 2025, 147:149918.

[14] Ren Y, Sun X, Qi K, Zhao Z. Single atom supported on MoS_2 as efficient electrocatalysts for the CO_2 reduction reaction: a DFT study. *Appl. Surf. Sci.* 2022, 602:154211.

[15] Li Z, Wang P, Lyu X, Kondapalli VKR, Xiang S, *et al*. Directing CO_2 electroreduction pathways for selective C_2 product formation using single-site doped copper catalysts. *Nat. Chem. Eng.* 2024, 1(2):159–169.

[16] Yang L, Li B, Wang RY, Meng Y, Tang YL, *et al*. Importance of local coordination microenvironment in regulating CO_2 electroreduction catalyzed by Cr-corrole-based single-atom catalysts. *J. Colloid Interface Sci.* 2025, 696:137856.

[17] Zhu H, Guo Z, Lan D, Liu S, Liu M, *et al*. Accelerating the design of catalysts for CO_2 electroreduction to HCOOH: a data-driven DFT-ML screening of dual atom catalysts. *J. Energy Chem.* 2024, 99:627–635.

[18] Zhu X, Yu J, Liu Y, Song Y, Zhang L, *et al*. Application of artificial intelligence combined with density functional theory in materials. *AI Mater.* 2026, 2(1):0001.

[19] Chen KX, Wang Y, Dong YQ, Zhao ZH, Zang Y, *et al*. Theoretical design of dual-site metallo-covalent organic frameworks for efficient CO_2 photoreduction into C_2H_4. *Appl. Catal. B: Environ. Energy* 2025, 365:124933.

[20] Ren C, Li Q, Ling C, Wang J. Mechanism-guided design of photocatalysts for CO_2 reduction toward multicarbon products. *J. Am. Chem. Soc.* 2023, 145(51):28276–28283.

[21] Ren C, Lu S, Wu Y, Ouyang Y, Zhang Y, *et al*. A universal descriptor for complicated interfacial effects on electrochemical reduction reactions. *J. Am. Chem. Soc.* 2022, 144(28):12874–12883.

[22] Wang Y, Wang Q, Wang X, Yang J, Jiang J, *et al*. Accelerated design of dual-metal-site catalysts via machine-learning prediction. *J. Phys. Chem. Lett.* 2025, 16(6):1424–1431.

[23] Qi C, Wang W, Lv K, Li D, Liu Y, *et al*. Catalytic applications of 2D materials aided by machine learning. *AI Mater.* 2025, 1(2):0014.

[24] Zhou J, Gu Z, Wang X, Zhang X, Ouyang Y, *et al*. Screening of single-atom catalysts for CO_2 electroreduction to CH_4 using DFT calculations and machine learning. *J. Mater. Chem. A* 2025, 13(29):24073–24083.

[25] Zhang XL, Chen M, Chen WX, Fang LC, Zhuang GL. Impact of 3d-metals on M-Pt@Cu dual-atom alloy for CO_2 electroreduction: Scaling descriptors. *Mol. Catal.* 2025, 573:114845.

[26] Xi S, Zhao P, He C, Zhang W. High-throughput screening of single-atom catalysts on 1T-TMD for highly active and selective CO_2 reduction reaction: computational and machine learning insights. *J. Catal.* 2024, 436:115610.

[27] Ouyang R, Ahmetcik E, Carbogno C, Scheffler M, Ghiringhelli LM. Simultaneous learning of several materials properties from incomplete databases with multi-task SISSO. *J. Phys.: Mater.* 2019, 2(2):024002.

[28] Ouyang R, Curtarolo S, Ahmetcik E, Scheffler M, Ghiringhelli LM. SISSO: a compressed-sensing method for identifying the best low-dimensional descriptor in an immensity of offered candidates. *Phys. Rev. Mater.* 2018, 2(8):083802.

[29] Kresse G, Furthmuller J. Efficient iterative schemes for ab initio total-energy calculations using a plane-wave basis set. *Phys. Rev. B* 1996, 54(16):11169–11186.

[30] Perdew JP, Burke K, Ernzerhof M. Generalized gradient approximation made simple. *Phys. Rev. Lett.* 1996, 77(18):3865–3868.

[31] Kresse G, Joubert D. From ultrasoft pseudopotentials to the projector augmented-wave method. *Phys. Rev. B* 1999, 59(3):1758–1775.

[32] Ringe S, Hormann NG, Oberhofer H, Reuter K. Implicit solvation methods for catalysis at electrified interfaces. *Chem. Rev.* 2022, 122(12):10777–10820.

[33] Mathew K, Kolluru VSC, Mula S, Steinmann SN, Hennig RG. Implicit self-consistent electrolyte model in plane-wave density-functional theory. *J. Chem. Phys.* 2019, 151(23):234101.

[34] Grimme S, Antony J, Ehrlich S, Krieg H. A consistent and accurate ab initio parametrization of density functional dispersion correction (DFT-D) for the 94 elements H-Pu. *J. Chem. Phys.* 2010, 132(15):154104.

[35] Monkhorst HJ, Pack JD. Special points for Brillouin-zone integrations. *Phys. Rev. B* 1976, 13(12):5188–5192.

[36] Tang W, Sanville E, Henkelman G. A grid-based Bader analysis algorithm without lattice bias. *J. Phys.: Condens. Matter* 2009, 21(8):084204.

[37] Maintz S, Deringer VL, Tchougreeff AL, Dronskowski R. LOBSTER: A tool to extract chemical bonding from plane-wave based DFT. *J. Comput. Chem.* 2016, 37(11):1030–1035.

[38] Dronskowski R, Bloechl PE. Crystal orbital Hamilton populations (COHP): energy-resolved visualization of chemical bonding in solids based on density-functional calculations. *J. Phys. Chem.* 1993, 97(33):8617–8624.

[39] Zhang F, Gong L, Liu M, Ying Y, Cui Y, *et al*. Nature of C-C coupling and strategy of tuning the catalytic activity of Cu-N-C catalysts for electro-reduction of CO_2 to ethanol. *Nano Energy* 2024, 127:109699.

[40] Wang V, Xu N, Liu JC, Tang G, Geng WT. VASPKIT: a user-friendly interface facilitating high-throughput computing and analysis using VASP code. *Comput. Phys. Commun.* 2021, 267:108033.

[41] Huang R, Hanif MF, Siddiqui MK, Hanif MF, Petros FB. Analyzing boron oxide networks through Shannon entropy and Pearson correlation coefficient. *Sci. Rep.* 2024, 14(1):26552.

[42] Chicco D, Warrens MJ, Jurman G. The coefficient of determination R-squared is more informative than SMAPE, MAE, MAPE, MSE and RMSE in regression analysis evaluation. *PeerJ Comput. Sci.* 2021, 7:e623.

[43] Schutte WJ, De Boer JL, Jellinek F. Crystal structures of tungsten disulfide and diselenide. *J. Solid State Chem.* 1987, 70(2):207–209.

[44] Tong L, Zhang B, Zhang Y, Peng Z, Fu X. Edge engineering on layered WS2 toward the electrocatalytic reduction of CO_2: a first principles study. *Phys. Chem. Chem. Phys.* 2022, 24(48):30027–30034.

[45] Kolle JM, Fayaz M, Sayari A. Understanding the effect of water on CO_2 adsorption. *Chem. Rev.* 2021, 121(13):7280–7345.

[46] He Y, Yin L, Yuan N, Zhang G. Adsorption and activation, active site and reaction pathway of photocatalytic CO_2 reduction: a review. *Chem. Eng. J.* 2024, 481:148754.

[47] Singh PP, P A, Kamaliny S, Ray K, Sengupta S. The pivotal role of oxygen vacancy and surface hydroxyl in the adsorption and activation of CO_2 on ceria-zirconia mixed oxide. *Mol. Catal.* 2024, 555:113855.

[48] Yu L, Li F, Huang J, Sumpter BG, Mustain WE, *et al*. Double-atom catalysts featuring inverse sandwich structure for CO_2 reduction reaction: a synergetic first-principles and machine learning investigation. *ACS Catal.* 2023, 13(14):9616–9628.

[49] Gao D, Ma L, Yang Y, Liu Z, Yu Y, *et al*. Breaking the linear scaling relationship in BN-supported metal catalysts for efficient CO_2RR towards C_1 and C_2 products. *J. Mater. Sci. Technol.* 2025, 224:172–182.

[50] Xu Y, Wang C, Liu S. d-electron modulated CO_2 electroreduction performance: Insights from T-carbon supported single-atom catalysts. *Mater. Today Chem.* 2026, 52:103444.

[51] Liu H, Yu Z, Zhao J, Ip WF, Lin S, *et al*. Electrochemical CO_2 reduction on Janus dual-atom catalysts: Critical role of oxygen coordination and an effective descriptor. *Adv. Sci.* 2025, 12(36):e07849.

[52] Guo X, Zhang H, Yang H, Bo Z, Yan J, *et al*. Single Ni supported on $Ti_3C_2O_2$ for uninterrupted CO_2 catalytic hydrogenation to formic acid: A DFT study. *Sep. Purif. Technol.* 2021, 279:119722.
[53] Hu S, Qiao P, Yi X, Lei Y, Hu H, *et al*. Selective photocatalytic reduction of CO_2 to CO mediated by silver single atoms anchored on tubular carbon nitride. *Angew. Chem. Int. Ed.* 2023, 62(26):e202304585.
[54] Ji W, Xie H, Deng B, Yu Y, Geng Q, *et al*. Cu metal-modified Nb_2O_5 microspheres boost photoreduction of CO_2 to CH_4 via enhanced adsorption of C1 intermediates. *Ind. Eng. Chem. Res.* 2025, 64(16):8248–8256.
[55] Lin Q, Zhao J, Zhang P, Wang S, Wang Y, *et al*. Highly selective photocatalytic reduction of CO_2 to CH4 on electron-rich Fe species cocatalyst under visible light irradiation. *Carbon Energy* 2024, 6(1):e435.
[56] Shen C, Meng XY, Zou R, Sun K, Wu Q, *et al*. Boosted sacrificial-agent-free selective photoreduction of CO_2 to CH_3OH by rhenium atomically dispersed on indium oxide. *Angew. Chem. Int. Ed.* 2024, 63(18):e202402369.
[57] Du H, Fu Y, Shi R, Cao Z, Zhang S, *et al*. Spatially separated C-C coupling and protonation on Cl-bridged Ti-Ag dual-site catalysts for efficient photocatalytic CO_2 reduction to C_2H_4. *Angew. Chem. Int. Ed.* 2026, 65(3):e20354.
[58] Zhang H, Yohannes A, Zhao H, Li Z, Xiao Y, *et al*. Photocatalytic asymmetric C–C coupling for CO_2 reduction on dynamically reconstructed $Ru^{\delta+}$-O/Ru^0-O sites. *Nat. Commun.* 2025, 16(1):534.
[59] Li X, Li Y, Li P, Yuan D, Fu Y, *et al*. Investigation of *COOH versus HCOO* intermediate by metallic Co-catalyst for selective photocatalytic reduction of CO_2 to CO. *Mol. Catal.* 2025, 585:115356.
[60] LeCun Y, Bengio Y, Hinton G. Deep learning. *Nature* 2015, 521(7553):436–444.
[61] Hawkins DM. The problem of overfitting. *J. Chem. Inf. Comput. Sci.* 2004, 44(1):1–12.
[62] Zafari M, Kumar D, Umer M, Kim KS. Machine learning-based high throughput screening for nitrogen fixation on boron-doped single atom catalysts. *J. Mater. Chem. A* 2020, 8(10):5209–5216.
[63] Zafari M, Nissimagoudar AS, Umer M, Lee G, Kim KS. First principles and machine learning based superior catalytic activities and selectivities for N_2 reduction in MBenes, defective 2D materials and 2D π-conjugated polymer-supported single atom catalysts. *J. Mater. Chem. A* 2021, 9(14):9203–9213.
[64] Qin H, Zhang H, Wang X, Fan W. Theoretical and experimental studies of CO_2 hydrogenation to methanol on TM/In_2O_3-ZrO_2 catalysts (TM = Cu, Ni and Pd): Mechanism analysis and quantitative description of MSI. *J. Catal.* 2024, 436:115586.
[65] Wang Y, Tian Y, Rennison AP, Blennow A, Westh P, *et al*. Applying the Sabatier principle to decipher the surface-structure-dependent catalysis of different starch granules by pullulanase. *JACS Au* 2025, 5(1):55–60.
[66] Wen X, Prezhdo OV, Xu L. Design of twisted two-dimensional heterostructures and performance regulation descriptor for electrocatalytic ammonia production from nitric oxide. *J. Am. Chem. Soc.* 2025, 147(17):14647–14658.
[67] Zhang J, Hu C, Li H, Li Q, Zhang Q, *et al*. A lead-free double perovskite $Cs_2AgBiBr_6$/BiOBr S-scheme heterojunction with enhanced Bi–Br–Bi coordination for photocatalytic CO_2 reduction. *Green Chem.* 2026, 28(15):6819–6829.

[68] Lum Y, Ager JW. Evidence for product-specific active sites on oxide-derived Cu catalysts for electrochemical CO_2 reduction. *Nat. Catal.* 2019, 2(1):86–93.

[69] Sun M, Ma Y, Tan Y, Wang J, Mi G, *et al*. Resolving charge recombination and intermediate stabilization: a rational design of In_2O_3/TiO_2 S-scheme heterojunction for efficient CH_4 production. *SusMat* 2025, 5(4):e70011.